Optical and electronic properties of 2H-MoS_2 under pressure: Revealing the spin-polarized nature of bulk electronic bands

Mauro Brotons-Gisbert,[1] Alfredo Segura,[1] Roberto Robles,[2] Enric Canadell,[3] Pablo Ordejón,[2] and Juan F. Sánchez-Royo[1,*]

[1]*Instituto de Ciencia de Materiales (ICMUV), Departamento de Física Aplicada, Universidad de Valencia, P.O. Box 22085, 46071 Valencia, Spain*

[2]*Catalan Institute of Nanoscience and Nanotechnology (ICN2), CSIC and BIST, Campus UAB, Bellaterra, 08193 Barcelona, Spain*

[3]*Institut de Ciència de Materials de Barcelona (ICMAB-CSIC), Campus de la UAB, 08193 Bellaterra, Barcelona, Spain*

(Received 13 November 2017; revised manuscript received 22 February 2018; published 11 May 2018)

Monolayers of transition-metal dichalcogenide semiconductors present spin-valley locked electronic bands, a property with applications in valleytronics and spintronics that is usually believed to be absent in their centrosymmetric (as the bilayer or bulk) counterparts. Here we show that bulk 2H-MoS_2 hides a spin-polarized nature of states determining its direct band gap, with the spin sequence of valence and conduction bands expected for its single layer. This relevant finding is attained by investigating the behavior of the binding energy of *A* and *B* excitons under high pressure, by means of absorption measurements and density-functional-theory calculations. These results raise an unusual situation in which bright and dark exciton degeneracy is naturally broken in a centrosymmetric material. Additionally, the phonon-assisted scattering process of excitons has been studied by analyzing the pressure dependence of the linewidth of discrete excitons observed at the absorption coefficient edge of 2H-MoS_2. Also, the pressure dependence of the indirect optical transitions of bulk 2H-MoS_2 has been analyzed by absorption measurements and density-functional-theory calculations. These results reflect a progressive closure of the indirect band gap as pressure increases, indicating that metallization of bulk MoS_2 may occur at pressures higher than 26 GPa.

DOI: 10.1103/PhysRevMaterials.2.054602

I. INTRODUCTION

The property that makes monolayers (MLs) of transition-metal dichalcogenide (TMD) semiconductors (such as MoS_2, $MoSe_2$, WS_2, and WSe_2) unique among two-dimensional (2D) materials is the unusual combination of strong spin-orbit interactions, broken inversion symmetry, and time-reversal symmetry [1,2]. The restrictions that they altogether impose can promote that the spin polarization of degenerate electronic states is reversed between states at $\mathbf{k}$ and $-\mathbf{k}$ in these MLs, which makes possible a selective photoexcitation of carriers in the K and K' valleys by using left or right circularly polarized light, respectively [1,3], as well as the observation of the valley Hall effect [4] and the realization of polarization-sensitive polaritonic devices operating at room temperature [5]. Collaterally, this particular property of these 2D materials has sowed the seeds for the search of new kinds of 2D ferroic systems [6], Weyl fermions [7], and topological superconductors [8]. Also, potential spintronic applications of 2D TMDs are very promising [9,10]. Spin splitting between the two highest valence bands at the K point (Δ_v) are known to be hundreds of meV [1–3]. However, for spintronic applications based on n-type 2D TMDs, it would be required to have a precise knowledge of the spin-polarization degree of their conduction bands and relatively large conduction-band spin-splitting (Δ_c) values. In this sense, a precise determination of Δ_c is also relevant to elucidate the dark/bright nature of excitons in 2D TMDs [11–14], which plays an important role in exciton lifetimes and quantum efficiencies for optical recombination processes [15–17]. Only recently, experimental studies on the spin sequence of conduction bands and Δ_c values have been reported for MLs of WSe_2, $MoSe_2$, and MoS_2 [18–20], giving results consistent with calculations [12,21,22].

It is usually believed that the spin polarization of the electronic bands of TMDs naturally emerges, only, in 2D TMDs with an odd number of layers and that it is absent in 2H-MoS_2 [23]. However, it has been suggested that hidden forms of spin polarization can exist even in centrosymmetric crystals under the condition that the spin-polarized bands are spatially localized apart from each other [24,25]. This interesting possibility would open the door to explore technological implications of the spin-polarized nature of TMDs not only in MLs but also in bilayers or bulk forms. Spin-polarized and angle-resolved photoemission techniques have provided for a direct evidence of the existence of a hidden spin texture in the valence bands of centrosymmetric WSe_2 [26] and in 2H-MoS_2 by using left- and right-handed circularly polarized light [27]. However, photoemission is a surface-sensitive technique that mostly probes the outermost layer, in which the inversion symmetry is broken and the interlayer effects are partly removed.

In this work, we have studied the optical and electronic properties of 2H-MoS_2 by optical absorption measurements under high pressure and density functional theory (DFT) calculations. This study has allowed us to approach the question of the hidden spin-polarized nature of the bulk valence and conduction bands. By applying pressure, we experimentally and theoretically demonstrate that the pressure dependence of the

*Juan.F.Sanchez@uv.es

excitonic optical transitions—specifically, the exciton binding energy (BE)—can be only understood by considering that the two highest valence bands and the two lowest conduction bands at the K (K') points are spin polarized, with a spin sequence that agrees with that expected by calculations reported so far for its ML. Moreover, our results evidence that the hidden spin-polarized nature of 2H-MoS_2 also conveys the rarely observed lift of the degeneracy between bright and dark excitons in a centrosymmetric material. Besides, relevant questions related to the phonon-assisted scattering process for A and B excitons and the evolution of the indirect band gap (E_g^{ind}) of bulk 2H-MoS_2 under pressure, have been also approached.

II. SPIN-VALLEY POLARIZATION OF ELECTRONIC BANDS OF 2H-MoS_2

A. Pressure dependence of optical-absorption coefficient of 2H-MoS_2

High-pressure techniques are particularly efficient in tuning the strength of interlayer interactions and elucidating their effects on the electronic and optical properties of layered materials [28]. In fact, from the point of view of the interlayer interactions in layered materials, high-pressure and exfoliation techniques are two sides of the same coin. The fundamental optical-absorption edge of 2H-MoS_2 has been measured in a 0.13-μm-thick sample under different hydrostatic pressure conditions, ranging between ambient pressure and 13 GPa [Fig. 1(a)]. The two well established A and B direct excitonic transitions of MoS_2 are clearly observed at ambient pressure [29,30], as well as a high-energy tail labeled as C that has been attributed to high-energy transitions occurring between states located at midpoint along the ΓK high-symmetry direction [31,32]. As pressure increases, the A and B excitonic peaks blueshift and broaden, being no longer observable at pressures higher than 10 and 8 GPa, respectively, whereas the C feature redshifts with no remarkable changes in shape. Upon decreasing pressure [top spectrum in Fig. 1(a)] the excitonic peaks are fully recovered, indicating that pressure-induced defects are not responsible for the disappearance of the excitonic peaks observed at high pressure. The absorption coefficient spectra showed in Fig. 1(a) have been analyzed in the frame of the Elliott-Toyozawa model [33,34] for a direct absorption including electron-hole interaction and considering a Gaussian broadening of the direct exciton line shapes due to the strong electron-phonon interaction in MoS_2 [35]. This model has been largely employed in the literature to successfully describe the optical-absorption edge of diamond or zinc-blende [36–38] and layered [39–42] semiconductors as well as 2D quantum-well systems [43,44]. In the frame of the Elliott-Toyozawa model [33,34], the absorption coefficient (α_{E-T}) can be expressed as

$$\alpha_{E-T}(E) = \frac{C_{0A}R_A^{1/2}}{E}\left\{\sum_{m=1}^{\infty}\frac{2R_A}{m^3}\frac{1}{\sigma_{mA}\sqrt{2\pi}}e^{-(E-E_{mA})^2/2\sigma_{mA}^2} + \int_{E_{0A}}^{\infty}dE'\frac{1}{1-e^{-2\pi\sqrt{\frac{R_A}{E'-E_{0A}}}}}\frac{1}{\sigma_{c,A}\sqrt{2\pi}}e^{(E'-E)^2/2\sigma_{cA}^2}\right\}$$
$$+\frac{C_{0B}R_B^{1/2}}{E}\left\{\sum_{m=1}^{\infty}\frac{2R_B}{m^3}\frac{1}{\sigma_{mB}\sqrt{2\pi}}e^{-(E-E_{mB})^2/2\sigma_{mB}^2} + \int_{E_{0B}}^{\infty}dE'\frac{1}{1-e^{-2\pi\sqrt{\frac{R_B}{E'-E_{0B}}}}}\frac{1}{\sigma_{c,B}\sqrt{2\pi}}e^{(E'-E)^2/2\sigma_{cB}^2}\right\}, \quad (1)$$

where A and B subindices refer to each one of the direct excitonic transitions. The integral terms in Eq. (1) represent the contribution of both excitonic continuums to the absorption coefficient. In Eq. (1), $C_{0A;B}$ are the absorption-strength parameters of the direct excitonic transitions, $R_{A;B}$ are the exciton Rydberg energies, $E_{0A;B}$ are the band-to-band direct transition energies, $E_{mA;B}$ represent the energy of the discrete m-excitonic transitions. The $\sigma_{cA;B}$ and $\sigma_{mA;B}$ variances can be related to the exciton continuum half widths ($\Gamma_{cA;B} = \sqrt{2\ln 2}\sigma_{cA;B}$) and the half width of the discrete exciton lines ($\Gamma_{mA;B} = \sqrt{2\ln 2}\sigma_{mA;B}$), respectively. For the $\Gamma_{mA;B}$ of the discrete m exciton, the empirical relationship $\Gamma_{mA;B} = \Gamma_{cA;B} - (\Gamma_{cA;B} - \Gamma_{1A;B})/m^2$ has been used [45]. In order to account for the contribution to the absorption coefficient of the high-energy tail [the C feature identified in Fig. 1(a)], a Gaussian-broadened steplike function occurring at the energy E_{0C} has been added to Eq. (1), as a first approximation to the line shape of the C feature. Under these assumptions, the absorption coefficient (α) can be expressed as

$$\alpha(E) = \alpha_{E-T}(E) + \frac{C_{0C}}{1+e^{(E_{0C}-E)/\Gamma_{CC}}}, \quad (2)$$

where C_{0C} is a proportionality constant, and Γ_{CC} is the width of the steplike direct transitions continuum band edge.

A word should be said about the Gaussian line shape adopted here to describe the exciton-phonon interaction in Eq. (1), in contrast to the Lorentzian one commonly used in high quality bulk crystals [37–39]. It is commonly accepted that compositional disorder, width fluctuations, and other kinds of disorder can promote inhomogeneous broadening of excitons, which turn the exciton line shape into a Gaussian line shape [44]. Although good-quality MoS_2 crystals have been used in our work, the relatively high BE values of A and B excitons in MoS_2, compared to other nonlayered semiconductors, makes the Bohr radius of excitons much lower than these of nonlayered semiconductors. Consequently, excitons in 2H-MoS_2 seem to be better described as Frenkel excitons rather than Wannier excitons, and then with an intrinsic phonon-exciton interaction better described by inhomogeneous broadening, as disorder can promote but extrinsically.

Taking into account these remarks, Eq. (2) has been used to analyze the experimental absorption-coefficient curves shown in Fig. 1(a). It should be noticed here that discrete excitonic terms with $m > 3$ have been neglected in these analyses. To conduct further discussion, the inset of Fig. 1(a) illustrates the results of fitting Eq. (2) to the absorption coefficient measured at a selected pressure of 5.07 GPa, in which the different contributions to the fitting curve are detailed. Curves labeled I and II represent the contributions (discrete and continuous) of

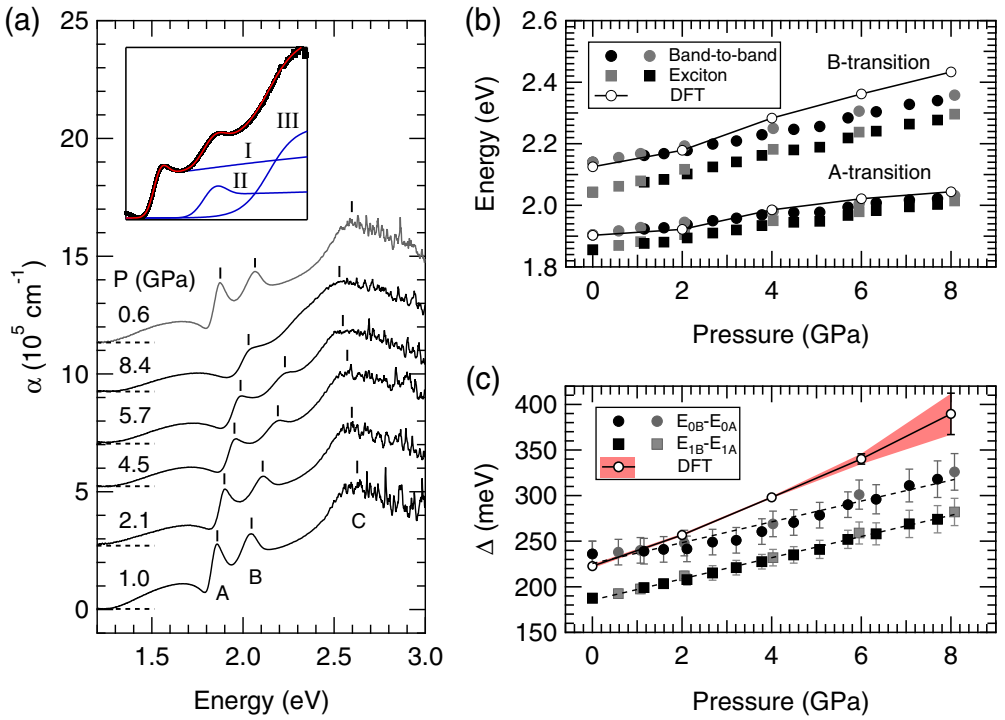

FIG. 1. (a) Fundamental absorption edge of 2H-MoS_2 measured under different applied hydrostatic pressures. Evolution with pressure of the identified *A*, *B*, and *C* features has been indicated by small solid bars. The inset shows an example of the result of fitting Eq. (2) to the absorption coefficient measured at the selected pressure of 5.07 GPa (red solid line). Each one of the contributions to the fitting curve has been included in the inset (blue solid lines), these corresponding to transitions involving states from the highest (I) and the next (II) valence bands at the *K* point, as well as these attributable to transitions located around the midpoint of the Γ*K* high-symmetry direction (III). (b) Pressure dependence of the energies of the *A* and *B* band-to-band direct transitions ($E_{0A;B}$) and the ground A_1 and B_1 excitonic transitions ($E_{1A;B}$), respectively, as extracted from the fitting of Eq. (2) to the experimental results showed in (a). Black and grey symbols represent values obtained in experiments in which hydrostatic pressure increases or decreases, respectively. Error intervals, as extracted from the fitting of Eq. (2) to the experimental data in Fig. 1(a), are smaller than the dimensions of the data points. The pressure dependence of the *A* and *B* band-to-band direct transitions, those obtained by DFT calculations, have been included. (c) Pressure dependence of the total band splitting $\Delta = E_{0B} - E_{0A}$ at the *K* point of 2H-MoS_2, as obtained from the experimental results collected in (b) (grey and black symbols). Error intervals have been propagated from data shown in (b). Open circles represent the pressure dependence of Δ_v, as obtained by DFT calculations. Since, *a priori*, optical direct transitions may occur from the two highest valence bands to each one of the two lowest conduction bands at the *K* point, the pressure dependence of Δ may be expected to evolve between $\Delta_v + |\Delta_c|$ [as would correspond to the MoS_2-like configuration illustrated in Fig. 3(a)] and $\Delta_v - |\Delta_c|$ [i.e., as the WSe_2-like configuration illustrated in Fig. 3(a)]. The range of Δ comprised between these two cases has been indicated by a light-red area and vertical errorlike bars, as obtained by DFT. For comparison purposes, the pressure dependence of the difference $E_{1B} - E_{1A}$ has been included in this plot, as extracted from the data shown in (b). Dashed lines are linear fits to the experimental data.

A and *B* excitons, respectively. The curve labeled III represents the contribution of the *C* feature. We would like to stress that, although the absorption coefficient spectrum of 2H-MoS_2 has been measured here for pressures as high as 13 GPa, we have restricted our analysis to the range of pressure in which both *A* and *B* excitons can be clearly identified and distinguished from the redshifting *C* feature (i.e., in the 0–8-GPa range). In fact, it can be noticed that, in the absorption coefficient spectrum measured at 8.4 GPa [Fig. 1(a)], only the *A* exciton can be clearly resolved. Therefore, proceeding in this way for all the absorption coefficient spectra acquired in the range 0–8 GPa [Fig. 1(a)], the pressure dependence of some relevant parameters has been obtained, in particular, the E_{0C}, the half width (Γ_{1A} and Γ_{1B}), and energies (E_{1A} and E_{1B}) of the ground *A* and *B* exciton lines, respectively, and the band-to-band direct transition energies E_{0A} and E_{0B} corresponding to the *A* and *B* transitions, respectively. In the following subsections, we focus on the analysis of the pressure dependence of the band-to-band and excitonic transitions, whereas results related with the pressure dependence of exciton linewidth and the E_{0C} feature will be discussed later.

B. Pressure dependence of the direct band gap

Unlike the A_1 and B_1 excitons [28,29,46], some lacuna exists for data related to the pressure dependence of band-to-band transitions, especially for these involving the *B* valence band. From our results [Fig. 1(b)], E_{0A} appears to be 1.904 ± 0.005 eV and $E_{0B} = 2.140 \pm 0.010$ eV at ambient pressure, in very good agreement with recently reported values [47]. In the range of pressure approached in this study, both E_{0A} and E_{0B} quasilinearly increase, with pressure coefficients of 15.5 ± 0.4 and 27.2 ± 0.7 meV/GPa respectively. From these results, the pressure dependence of the total band splitting $\Delta = \Delta_c + \Delta_v = E_{0B} - E_{0A}$ can be obtained [Fig. 1(c)]. A value of $\Delta = 236 \pm 15$ meV is experimentally obtained for

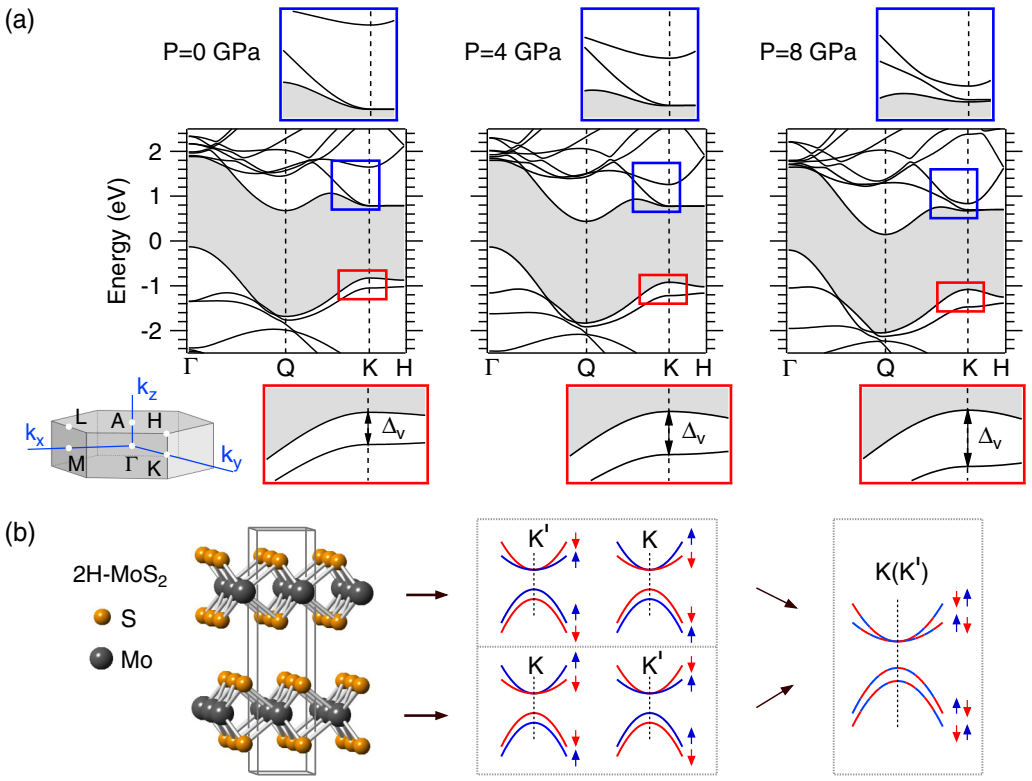

FIG. 2. (a) Electronic band structure of 2H-MoS_2 calculated by DFT along the Γ*K* and the *KH* high-symmetry directions of the Brillouin zone (also shown). Calculations have been performed at ambient conditions (left), 4 GPa (center) and 8 GPa (right). The top and bottom panels show zooms of the corresponding electronic conduction and valence bands located in the vicinity of the direct band gap of 2H-MoS_2, respectively. (b) Illustration of the spin-polarized nature of the electronic bands at the *K* (*K*′) point of each single layer composing the unit cell of 2H-MoS_2 (left side). The characteristics of these bands remain basically unaltered when two layers stack together due to their strongly localized nature, giving rise to energy and spin degenerate bands in the centrosymmetric material that retain spin information from layer of provenience (right side).

2H-MoS_2 at ambient pressure and in agreement with that obtained by angle-resolved photoemission [48], which evolves with pressure with a quasilinear pressure coefficient of 11.4 ± 0.6 meV/GPa. These results consistently extend the range of pressures approached by studies reported so far [28,49], providing for an accurate determination of the pressure coefficients of the direct band-to-band transitions of 2H-MoS_2 in a pressure range reaching 8 GPa.

Results shown in Figs. 1(b) and 1(c) can be understood by considering the tuning of interlayer interactions by means of pressure and their effects on the electronic properties of 2H-MoS_2. Figure 2(a), left side, shows the electronic band structure of bulk MoS_2 calculated at ambient conditions by DFT along the Γ*K* and the *KH* high-symmetry directions [see the hexagonal Brillouin zone of 2H-MoS_2 also depicted in Fig. 2(a)], in which spin-orbit coupling has been included. In line with other calculations reported [50–52], the electronic bands in the vicinity of the direct gap of MoS_2 show [top left and bottom left zoomed plots of Fig. 2(a), for the conduction and valence bands, respectively] two nearly degenerate conduction bands at the *K* point ($|\Delta_c| = 2$ meV at ambient pressure) with different effective masses along the Γ*K* direction ($m_\perp^*$) which are, importantly, strongly localized in the layer plane. With respect to the split valence bands at the *K* point, it is worth noting that their curvatures have the opposite sign along the *KH* direction. By increasing pressure until 8 GPa, our calculations show that the consequent enhancement of interlayer interactions appears not to alter the orbital nature nor the character of states at the edges of the conduction and valence bands at the *K* point [Fig. 2(a), middle and right plots], although an unoccupied Mo $d_{xz,yz}$ band [51,53] seems to approach the bottom of the conduction band as pressure increases. However, it is relevant to notice that the $m_\perp^*$ of the two lowest conduction bands at the *K* point, as calculated by DFT, evolve with pressure differently from each other (top plots of Fig. 2(a) and Fig. 8 of Appendix B). Besides the effective masses of states involved in the direct optical transitions, other important aspects of the electronic band structure appear to strongly depend on interlayer interactions; specifically, the direct band gap, the total band splitting ($\Delta = \Delta_v + \Delta_c$), and the E_g^{ind}. In spite of the lack of data available in the literature regarding the pressure dependence of the E_{0A} and E_{0B} direct transitions, the experimental results obtained [Fig. 1(b)] can be directly contrasted with the electronic band structure of 2H-MoS_2 calculated at different pressures [Fig. 2(a)]. The pressure dependence of both E_{0A} and E_{0B}, as obtained by DFT calculations, has been included in Fig. 1(b). The calculated values of $E_{0A;B}$ have been rigidly shifted by a constant value of 0.29 eV to take into account the well-known DFT underestimation of the band gap. Apart from this well-known band-gap offset, it appears that the DFT calculations

nicely reproduce the pressure dependence of E_{0A} and E_{0B} obtained experimentally. Also, our DFT calculations predict a band splitting of $\Delta \approx \Delta_v = 220$ meV at ambient pressure, which results from the combination of spin-orbit coupling and interlayer interactions. This value of Δ appears to be in very good agreement with that obtained experimentally [Fig. 1(c)].

C. Pressure dependence of the *A* and *B* excitonic transitions

Let us face now the pressure dependence of the exciton E_{1A} and E_{1B} energies [Fig. 1(b)]. The energies of the first excitonic transitions result in $E_{1A} = 1.855 \pm 0.002$ eV and $E_{1B} = 2.043 \pm 0.002$ eV at ambient pressure, following a quasilinear evolution as pressure increases until 8 GPa with pressure coefficients of 19.6 ± 0.5 and 31.2 ± 0.6 meV/GPa, which nicely agrees with early [54] and recent observations [28]. From these results, the difference in energy between the ground B and A excitonic transitions ($E_{1B} - E_{1A}$) has been obtained [Fig. 1(c)]. In MLs of MoS_2, this difference is usually adopted to estimate Δ_v ($\approx\Delta$). However, this approach is valid only if the BE of excitons A and B (BE_{1A} and BE_{1B}, respectively) are exactly the same, which is clearly not the case in bulk 2H-MoS_2 [28]. The $E_{1B} - E_{1A}$ difference can be expressed in terms of Δ, BE_{1A}, and BE_{1B} as $E_{1B} - E_{1A} = \Delta - (BE_{1B} - BE_{1A})$. Consequently, the fact that Δ and $E_{1B} - E_{1A}$ [Fig. 1(c)] give different values at each pressure and that they exhibit a different pressure dependence clearly indicates that A and B excitons have a different anisotropic degree and/or different exciton effective masses. This observation will play a key role to unravel, by means of optical-absorption measurements, the possible hidden spin-polarized nature of bulk electronic bands at the K point of 2H-MoS_2 [24–27]. DFT calculations predict (see Fig. 9 of Appendix C) a finite entanglement between spin, valley, and layer index at ambient pressure [24,25], for all valence and conduction states in the vicinity of the K point of 2H-MoS_2. Such a particular spin-valley-layer connection has been illustrated in Fig. 2(b): The electronic band structure of centrosymmetric TMDs remains, indeed, spin degenerate even in the presence of spin-orbit coupling. However, since the spin-orbit interaction does not couple orbitals of different layers [25], each single band of the bulk would be expected to preserve the spin and valley index of the atomic layer of provenience. Experimentally, optical absorption arises as a powerful technique to indirectly probe the possible spin-polarized nature of the bulk bands at the K point of 2H-MoS_2 since, in this material, direct optical-absorption transitions are, in essence, intralayer processes. This is based on the fact that, although wave functions of states determining the two highest valence bands at the K point exhibit some delocalization along the KH direction, the two lowest conduction bands are strongly localized in the layer plane [see Fig. 2(a) and Fig. 9 of Appendix C]. Consequently, the overlap between the Bloch wave functions of initial and final states required for optical-absorption processes is spatially limited within each atomic layer. Moreover, as optical-absorption techniques involve valence and conduction bands, the possible spin-polarized nature scheme described above appears to be naturally linked to the spin-band sequence of valence and conduction bands at the K point in 2D MoS_2 [12,19,21,22]. In a spin-degenerate case, two optically allowed (spin conserving) direct absorption processes may be expected to occur between each one of the valence bands and the two conduction bands at the K point of 2H-MoS_2 [Fig. 2(b), right side]. However, in the case that bulk valence and conduction bands retained the spin polarization of their ML constituents [12,21,22], only one of the two mutually exclusive possibilities indicated in Fig. 3(a) could take place, which correspond, for each one of these possibilities, to direct optical transitions attending a spin-band sequence in a WSe_2-like or in a MoS_2-like fashion [12,19–22]. Figure 3(b) shows the pressure dependence of the BE of excitons, as extracted from the results shown in Fig. 1(b). At ambient pressure, the BE of excitons is found to be $BE_{1A} = 49 \pm 7$ meV and $BE_{1B} = 97 \pm 10$ meV, which again agree with previous observations [30,53,55,56]. As pressure increases, the BE of both excitons decreases. A Gerlach-Pollmann model of an exciton has been adopted to interpretate these results [57], since the band dispersion of valence and conduction bands along the ΓK and KH high-symmetry directions are all highly anisotropic [Fig. 2(a)]. In the context of this model, the anisotropy parameter (β) is defined as

$$\beta = 1 - \frac{\mu_\perp \varepsilon_\perp(0)}{\mu_\parallel \varepsilon_\parallel(0)}, \tag{3}$$

where $\mu_\perp$ and $\mu_\parallel$ are the exciton reduced mass and $\varepsilon_\perp(0)$, and $\varepsilon_\parallel(0)$ are the static dielectric constant; both variables particularized for the perpendicular and parallel to the c-axis directions, respectively. In the isotropic case, $\beta = 0$ and $\beta < 0$ in bulk layered semiconductors such as InSe [58] or GaSe [45]. In the frame of this model, the BE of ground excitons can be written as

$$BE_1 = \mathrm{Ry}\frac{\mu_\perp}{\varepsilon_\perp(0)\varepsilon_\parallel(0)}[Z_{00}(\beta)]^2 \tag{4}$$

where Ry = 13.6 eV is the free-exciton Rydberg energy and the $Z_{00}(\beta)$ function is

$$\begin{aligned} Z_{00}(\beta) &= \frac{1}{\sqrt{\beta}}\arcsin\sqrt{\beta} && \text{for } \beta > 0, \\ Z_{00}(\beta) &= 1 && \text{for } \beta = 0, \\ Z_{00}(\beta) &= \frac{1}{\sqrt{|\beta|}}\operatorname{arcsinh}\sqrt{|\beta|} && \text{for } \beta < 0. \end{aligned} \tag{5}$$

In order to analyze the pressure dependence of the BE of A and B excitons, a precise knowledge of $\mu_\perp$, $\mu_\parallel$, $\varepsilon_\perp(0)$, and $\varepsilon_\parallel(0)$ is required. Our DFT calculations reveal a pressure dependence of $\mu_\perp$ and $\mu_\parallel$ that depend on the bands involved in the excitonic transition [see Figs. 8(b) and 8(c) of Appendix B] whereas $\varepsilon_\perp(0)$ and $\varepsilon_\parallel(0)$ have been shown to increase, theoretically and experimentally, as pressure increases (see Appendix D).

Before evaluating the BE of the A and B excitons in the frame of the Gerlach-Pollmann model, a word should be said about their respective Z_{00} function. From our results, it appears that the Z_{00} function varies between 1 and 1.25 for the A exciton in the pressure range comprised in this work, which indicates a moderately anisotropic behavior. However, the Z_{00} function evaluated for the B exciton gives imaginary numbers in the whole pressure range explored due to the rare combination of a valence band with a saddle point and a 2D conduction band at the K point [Fig. 2(a)]. This makes the B exciton better described by an extremely anisotropic exciton, basically 2D;

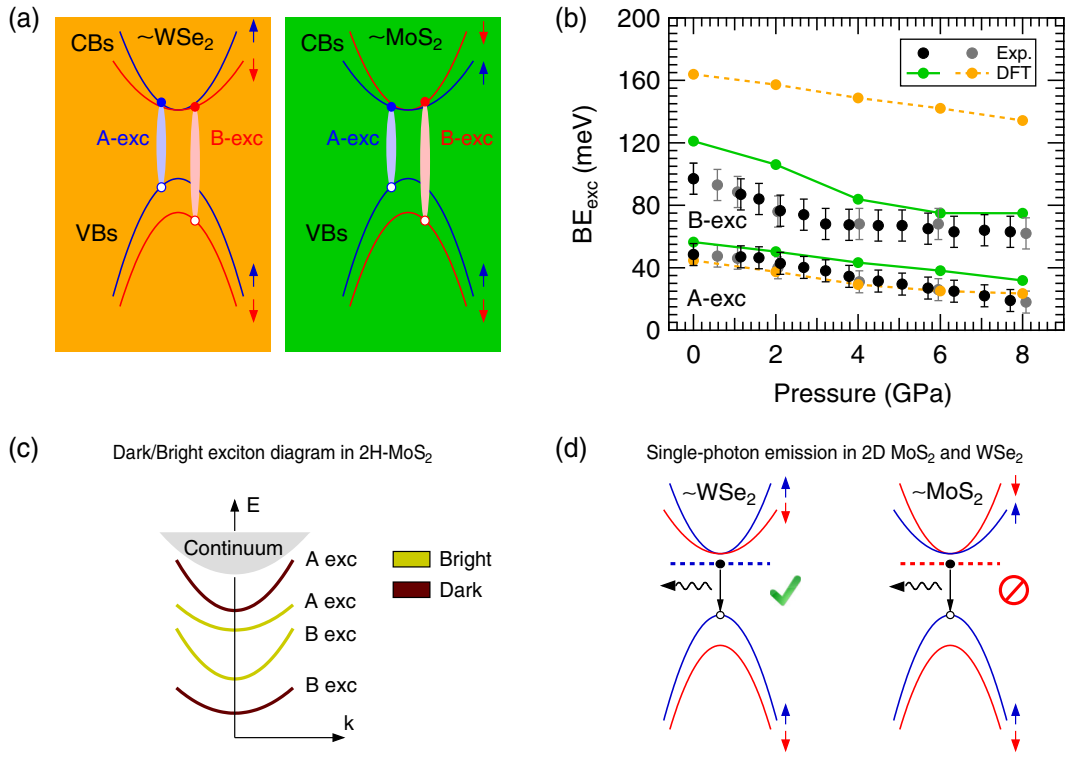

FIG. 3. (a) Schematic description of the two options of allowed A and B direct optical transitions, those following a WSe_2-like or a MoS_2-like spin-order configuration of a ML. (b) Pressure dependence of the BE of ground A and B excitons of 2H-MoS_2, as extracted from the results shown in Fig. 1(b) by using that $BE_{1A;B} = E_{0A;B} - E_{1A;B}$ (black and grey circles). Error intervals have been propagated from data shown in Fig. 1(b). The pressure dependence of the BE of the ground A and B excitons, as calculated in the frame of the Gerlach-Pollmann model, has been included. These calculations have been performed for each one of the two possible sets of optical transitions that have been considered in (a). The color code used to plot the results of these calculations is the same as that used for the background of illustrations shown in (a), i.e., orange for WSe_2-like excitons and green for MoS_2-like excitons. (c) Proposed scheme of the bright and dark distribution of A and B excitons in 2H-MoS_2, as obtained from the results shown in (a). (d) Illustration of the different radiative properties of eventual single-photon emitters in 2D TMDs based on W and Mo transition metals, provided that spin information of extended states remains unaltered when giving rise to impurity-related localized states.

then, although the case of a 2D exciton is not explicitly considered in the Gerlach-Pollmann model, it would correspond to the case of $Z_{00}(2D) = 2$ for any estimate of BE_{1B} by using this model.

By introducing the pressure dependence of of $\mu_\perp, \mu_\parallel, \varepsilon_\perp(0)$, and $\varepsilon_\parallel(0)$ obtained by DFT calculations (see Appendixes B and D) into Eqs. (4) and (5) and using a $Z_{00} = 2$ for the B_1 exciton, we have calculated the pressure dependence of the BE_1 of A and B excitons [Fig. 3(b)] for the WSe_2-like and MoS_2-like configurations [Fig. 3(a)]. By comparing these calculations with the experimental results, it appears that, although the pressure dependence of allowed optical transitions of the A exciton can be described by the two configurations illustrated in Fig. 3(a), these of the B exciton can be only associated to that corresponding to the MoS_2-like one. Therefore, since the possible options of spin-conserving excitonic transitions for the A and B excitons mutually exclude to each other, the MoS_2-like configuration shown in Fig. 3(a) appears to be the only one able to reproduce all experimental results described above. These results reveal that optical-absorption measurements under pressure in 2H-MoS_2 here reported share with photoemission the ability to probe excitation processes localized within a particular single layer [26,27], with the advantage of reflecting the properties of the bulk material instead of these of the topmost layer. Our results evidence, although indirectly, that spin-polarized bands exist in centrosymmetric MoS_2 at the K point. Moreover, our results reveal that the hidden spin texture of valence and conduction bands of 2H-MoS_2 follows a spin order that agrees with that predicted in its ML at ambient pressure [12,21,22]. These results, also, shed some light on the origin of nontrivial circular polarization degree of the photoluminescence signal observed in bilayer transition-metal dichalcogenides under circularly polarized excitation light [3,59–62].

The results summarized in Fig. 3(b) naturally reveal also an unusual lift of the bright/dark degeneracy of A and B excitons in a centrosymmetric material [Fig. 3(c)] that can be used as a platform for the study of the bright/dark nature of excitons in 2D materials [11–15]. From the results reported here, it appears that centrosymmetric MoS_2 varieties, such as the bilayer or bulk materials, are able to sustain bright and dark excitons [Fig. 3(c)] with a larger splitting energy between dark and bright states than in its ML due to a larger difference between the $\mu_\perp$ of A and B excitons although the two lowest conduction bands are almost degenerate at the K point [14]. Also, these results can eventually provide for a route to clarify if single

quantum emitters, on-demand emitters of one photon at a time into a given spatiotemporal mode [63], obey spin and valley optical selection rules of MLs of TMDs [Fig. 3(d)] [1–3]. An impurity or defect would be expected mainly to localize electronic states with larger spatial extension [64], i.e., electrons in conduction band states with a lower effective mass [Fig. 3(d)]. In this context, optical recombination processes from these localized states were expected to occur with a higher probability in W-based TMDs than in Mo-based ones, provided that localized states conserved the spin-polarized nature of the unperturbed ones. More work should be required to elucidate this question. However, this may explain the lack of reports demonstrating the existence of single-photon emitters in MLs of Mo-based TMDs [65], compared to those reported for the W-based ones [66–70].

The experimental results reported above and supported by our DFT calculations provide for strong evidences of an inherent spin-polarized nature of valence and conduction bands at the K point of 2H-MoS_2 at ambient pressure, which follows the spin-band sequence expected for 2D MoS_2. These evidences have been obtained by optical absorption and DFT techniques by using pressure as a variable to tune interlayer interactions, the curvature of mass of bands involved in optical transitions, and the dielectric constant of 2H-MoS_2, without using spin-valley sensitive techniques such as circularly polarized light [1,3]. Then, we would like to stress that our measurements are not directly spin sensitive. Keeping this in mind, it is worth noticing that our DFT calculations also predict that, as a consequence of subtle changes in the band structure induced by the increase of the interlayer interactions, not affecting the band dispersions, the material would be expected to experience an inversion of the spin-band sequence of its conduction bands, adopting a WSe_2-like configuration [Fig. 3(a)] at high pressure. From our DFT calculations, such a spin-flip transition would be expected at pressures around 4 GPa. However, much work should be performed, by using circularly polarized light, for instance, to clarify the possible existence of a pressure-induced spin-flip transition in 2H-MoS_2 and its onset.

III. PRESSURE DEPENDENCE OF THE *A* AND *B* EXCITON BROADENING

The pressure dependence of the Γ_1 half width of the A_1 and B_1 discrete exciton lines of 2H-MoS_2 has been estimated (Fig. 4), by fitting Eq. (2) to the experimental data shown in Fig. 1(a). The Γ_1 half widths of both excitons appear to exhibit a progressive and reversible broadening as pressure increases. At ambient pressure, values of 25.0 ± 0.5 and 40 ± 1 meV were found for Γ_{1A} and Γ_{1B}, respectively, which are in good concordance with reported values of the half width half maximum for the A_1 and B_1 exciton linewidths at 300 K [28,29,46]. The reversible broadening of the exciton linewidths observed with increasing pressure can be interpreted in terms of an increase of phonon-assisted scattering of electrons between the local conduction-band minimum at the K point and the absolute conduction-band minimum located at the Q point [37,38], i.e., at the midway along the ΓK high-symmetry direction. Such an increase of phonon-assisted scattering can be attributed to the relative downshift of the absolute conduction-band minimum observed [Fig. 2(a)] with respect

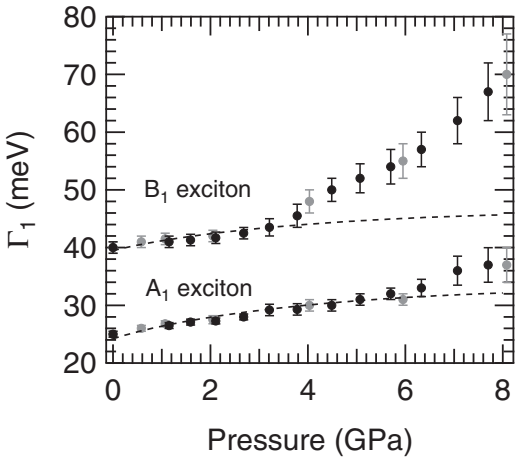

FIG. 4. Pressure dependence of the Γ_1 half width of the first excitonic peaks (A_1 and B_1 excitons) of the fundamental absorption edge of 2H-MoS_2. Dashed lines are fitting curves obtained by means of Eq. (6). Although these curves have been plotted in the whole 0–8-GPa range, the fitting processes have been performed in the range of pressure comprised between 0 and 6.5 GPa (A_1 exciton) and 0–4 GPa (B_1 exciton), to conduct further discussion.

to the local conduction-band minimum at the K point. In this way, A and B excitons, which are already resonant at ambient pressure, become more resonant as pressure increases. This pressure-induced broadening of the exciton lines, combined with the redshift of the high-energy absorption tail [the C feature identified in Fig. 1(a)] makes the B excitonic structure no longer observable for pressures above 8 GPa. The pressure dependence of Γ_{1A} and Γ_{1B} can be used to estimate the corresponding phonon deformation potential constant. Within the effective-mass approximation, the exciton linewidth induced by phonon scattering can be expressed, as a function of the energy difference between the conduction-band minima at the K and Q points (ΔE_{KQ}), as [37,38]:

$$\Gamma_{1A;B} = \Gamma_0 + \frac{N_Q m^{*3/2}_Q D^2_{KQ}}{\sqrt{2}h\rho\Omega_Q}[(n(\Omega_Q)+1)\sqrt{\Delta E_{KQ}-\Omega_Q} + n(\Omega_Q)\sqrt{\Delta E_{KQ}+\Omega_Q}], \quad (6)$$

where Γ_0 is a constant, h is Planck's constant, $\rho = 5.06\,\mathrm{g/cm^3}$ is the 2H-MoS_2 density, m^*_Q is the density-of-states effective mass of the conduction-band minimum at the Q point, $N_Q = 6$ is the number of equivalent indirect minima in the conduction band at the Q point, $n(\Omega_Q)$ and Ω_Q are the occupation number and energy of the phonons involved in the scattering, respectively, and D_{KQ} is the phonon deformation potential for intervalley phonon scattering. The pressure dependence of m^*_Q and ΔE_{KQ} has been extracted from band-structure calculations as those shown in Fig. 2(a). Recently, the nature of phonons responsible for intervalley scattering has been investigated in 2D MoS_2 and 2H-MoS_2 by means of double-resonance Raman spectroscopy and DFT calculations [71]. In that work, the authors found that longitudinal acoustic phonons (those with $\Omega_Q = 30$ meV) dominate intervalley scattering in this material. By using these parameters, fitting Eq. (6) to the experimental data shown in Fig. 4, in the range 0–6.5 and 0–4

GPa and for the A_1 and B_1 excitons, respectively, yields $D_{KQ} = 4.8 \pm 0.2\,eV/Å$ for the A_1 exciton and $D_{KQ} = 4.3 \pm 0.4\,eV/Å$ for the B_1 exciton. These values appear to be in line with those found for diamond and zinc-blende semiconductors [37,38].

These results evidence the strong role played by phonon-assisted scattering of electrons between the K and Q conduction-band minima to determine the lifetime of both A and B excitons from ambient pressure to 4 GPa, which may be relevant for valleytronic applications of MoS_2 [1–5]. However, it can be noticed that the B_1 exciton exhibits a more pronounced broadening than the A_1 exciton as pressure increases from 4 to 8 GPa (Fig. 4). This may be understood by the fact that the second lowest valence band at the Γ point upshifts in energy as pressure increases [Fig. 2(a)] and becomes resonant with states at the B valence band at the K point at 4 GPa. In consequence, an additional decay channel appears at 4 GPa for holes in the B valence band at the K point that is absent for holes at the A one, which enhances the pressure dependence of the Γ_1 of the B_1 exciton with respect to that of the A_1 exciton in the range of pressure comprised between 4 and 8 GPa. Only at pressures as high as ∼7 GPa do additional decay channels appear accessible also for A excitonic transitions since, at these high pressures, the second lowest valence band at the Γ point becomes resonant with A valence-band states at the K point [Fig. 2(a)].

IV. PRESSURE DEPENDENCE OF THE INDIRECT BAND GAP OF 2H-MoS_2

It has been theoretically predicted that MLs and bilayers of MoS_2 can metallize under strain [72,73]. Similarly, a pressure-induced closure of the E_g^{ind} has been predicted to appear in bulk TMDs due to the consequent enhancement of the interlayer interactions [50–52,74]. In the particular case of bulk TMDs, the determination of the metallization onset is particularly relevant for the fundamental point of view due to the possibility that exotic insulator states, such as the so-called excitonic insulator [75], may exist just before the metallization onset [51,76]. Experimentally, a pressure-induced metallic state has been observed to develop in bulk in WSe_2 [74] and in MoS_2 [77–79]. However, some controversy seems to exist for the pressure values reported so far for the onset of metallization, at least for MoS_2. On the one hand, electrical conductivity, x-ray-diffraction, and Raman spectroscopy measurements performed in 2H-MoS_2 show that 2H-MoS_2 becomes metallic at pressures higher than 40 GPa [78], after completion of an isostructural phase transition that starts at 20 GPa [78]. On the other hand, similar studies [77] and impedance and Raman spectroscopy measurements carried out in 2H-MoS_2 [79] reveal that 2H-MoS_2 becomes metallic at pressures close to 20 GPa, after a structural lattice distortion [77,79]. *Ab initio* DFT calculations predict a pressure-driven metallization onset around 20 GPa [77], which arises from the overlap of the valence and conduction bands owing to sulphur-sulphur interactions as the interlayer spacing reduces. Recently, some authors have proposed that experimental conditions (in particular, the pressure medium used) [79] or excess sulfur content [80] can affect the properties of structural layered materials under pressure, which may drastically determine structural changes that seem to precede metallization of 2H-MoS_2 [77–79].

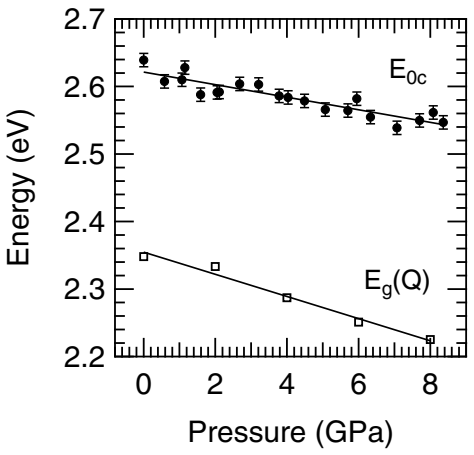

FIG. 5. Pressure dependence of high-energy excitonic transitions giving rise to the C-labeled feature identified in the curves showed in Fig. 1(a). Error intervals have been obtained by fitting Eq. (2) to the experimental data in Fig. 1(a). The pressure dependence of the band gap at the Q point has been included, as obtained from DFT band-structure calculations [Fig. 2(a)]. Solid lines are linear fitting curves.

In this section, we face the study of the pressure dependence of the E_g^{ind} of 2H-MoS_2 and its eventual pressure-driven metallization onset, by means of optical-absorption measurements under pressure. Results reported in the previous sections already envisage a progressive closure of the E_g^{ind} as pressure increases. In fact, the C-labeled feature [Fig. 1(a)] appears to redshift as pressure increases with no remarkable changes in shape. This feature has been attributed to direct transitions involving valence band states located in the proximity of the Q point, where both valence and conduction bands have a minimum and the parallel shape of the bands causes a maximum in the joint density of states [31,32]. This assignment of the C feature seems to be supported by our results. Figure 5 shows the pressure dependence of the E_{0C} related energy obtained by fitting Eq. (2) to the absorption coefficient spectra measured at different applied pressures [Fig. 1(a)]. In this figure, the pressure dependence of the band gap at the Q point has been included, as obtained from DFT band-structure calculations as those shown in Fig. 2(a). Comparing the pressure coefficient of the C feature (-9.3 ± 0.9 meV/GPa) and that of the band gap at the Q point (-16 ± 2 meV/GPa), it seems plausible that a progressive closure of the band gap of 2H-MoS_2 takes place as pressure increases [77–79].

In order to gain a deeper insight into the onset of the pressure dependence of the E_g^{ind} of 2H-MoS_2, we have performed optical transmittance measurements in bulk MoS_2 samples for pressures ranging from ambient conditions up to 26 GPa. An 11-μm-thick MoS_2 sample has been used for the measurements carried out between ambient conditions and 13.8 GPa, whereas for measurements between 15.7 and 26.1 GPa we have employed a thinner (1.2-μm thick) MoS_2 sample. Figure 6(a) shows some examples of the absorption edge measured in MoS_2 samples at hydrostatic pressures ranging from ambient pressure up to 26.1 GPa. As it can be observed in this figure, the indirect absorption edge of bulk MoS_2 shows a clear (and reversible) redshift with increasing pressure.

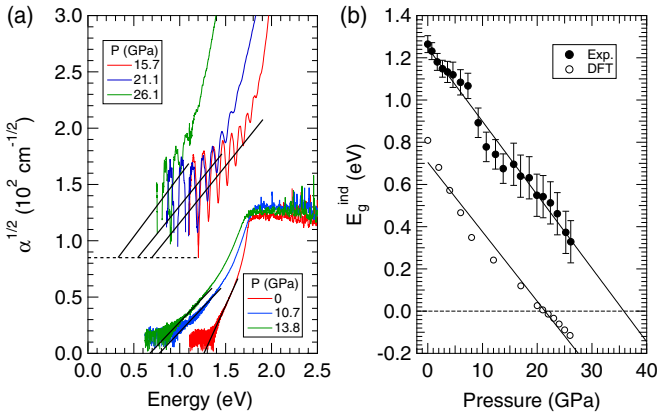

FIG. 6. (a) Square root of the absorption edge measured in 2H-MoS_2 samples 11 μm thick (bottom spectra) and 1.2 μm thick (top spectra) for pressures ranging from ambient conditions up to 26.1 GPa. Solid lines are linear fittings of $\alpha^{1/2}$ and extrapolated to $\alpha = 0$ to estimate the indirect band gap at each pressure. (b) Pressure dependence of the indirect band gap of 2H-MoS_2, as extracted from (a) (black circles) and as obtained by DFT calculations (open circles). Solid lines are linear fitting curves.

The optical E_g^{ind} energy for all studied pressures has been determined from the linear fits of the square root of the low-energy tail of the absorption edge. Figure 6(b) shows the pressure dependence of the optical E_g^{ind} resulting from these fittings. At room pressure, a value of $E_g^{ind} = 1.26 \pm 0.04$ eV has been found, which is in excellent agreement with that reported [54]. As shown in this figure, increasing hydrostatic pressure leads to a linear decrease of the optical E_g^{ind} from 1.26 eV at atmospheric pressure down to 0.33 eV at 26 GPa, with a pressure coefficient of -34.8 ± 1.8 meV/GPa.

The results shown in Fig. 6 reflect a progressive closure of E_g^{ind} which indicates that, at pressures close to 26 GPa, 2H-MoS_2 still remains semiconducting in contrast to some experimental results reporting a semiconductor-to-metal transition of 2H-MoS_2 at pressures close to 20 GPa [77,79]. In order to estimate the metallization onset of 2H-MoS_2, it would be tentative to extrapolate, towards higher pressures, the linear trend of E_g^{ind} observed as pressure increases until 26 GPa. To test the validity range of this procedure, we have calculated the electronic band structure of 2H-MoS_2 (Fig. 7) at different pressures, by means of DFT in the local-density approximation (LDA) [81]. As it can be observed in this figure, the uppermost valence band and the lowermost conduction band defining the indirect optical band gap of bulk MoS_2 experience a progressive upshift and downshift, respectively, with increasing pressure, which allows us to obtain an estimate of the pressure coefficient of the E_g^{ind}. At this point, it must be outlined that DFT-LDA calculations are known to provide for accurate relative trends of band gaps as a function of pressure [49,77]. However, these methods provide for absolute band-gap values that often differ from experimental ones in amounts that may vary from point to point of the reciprocal space and, consequently, give rise to inaccurate metallization-onset estimates [77]. To illustrate this, one can notice that our band-structure calculations predict $E_{0A} = 1.613$ eV, $E_{0B} = 1.835$ eV, and $E_g^{ind} = 0.805$ eV at ambient pressure [Fig. 2(a)]. These values are in excellent agreement with DFT calculations performed under similar approaches (see, for instance, Table 2 in Ref. [49]). However, these calculations underestimate experimental direct band gap and E_g^{ind} values by 0.30 eV [47] and 0.45 eV [54], respectively. Other DFT approaches can be used to obtain more accurate estimates of band-gap values [49]. However, structures are hard to be relaxed under these approximations.

In Fig. 6(b), the pressure dependence of the E_g^{ind} of 2H-MoS_2, as calculated by DFT-LDA has been included. These calculations indicate that the E_g^{ind} linearly diminishes as the pressure increases, with a pressure coefficient of -32.9 meV/GPa that nicely agrees with that extracted from the experimental trend [Fig. 6(b)]. Then, apart from the band-gap underestimation inherent in DFT-LDA calculations and discussed above, these results indicate that a semiconductor-to-metal transition in 2H-MoS_2 can be expected to occur at pressures higher than 26 GPa, with a metallization onset estimated around 35 GPa. These results seem to be in agreement with electrical conductivity, x-ray-diffraction, and Raman spectroscopy measurements performed in 2H-MoS_2 [78], which show that 2H-MoS_2 remains semiconducting at 28 GPa and becomes metallic at pressures higher than 40 GPa.

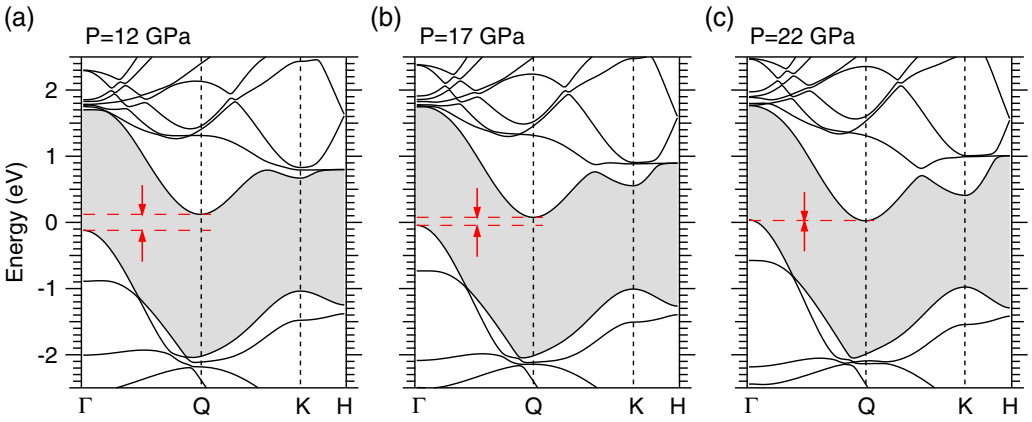

FIG. 7. Electronic band structure of 2H-MoS_2 calculated by DFT along the ΓK and the KH high-symmetry directions at 12 GPa (left), 17 GPa (center), and 22 GPa (right). Note the progressive closure of the indirect band gap as pressure increases, indicated by red dashed lines.

V. CONCLUSION

In summary, results here reported open the door for valleytronic and spintronic applications of not only MLs of MoS_2 but also its bilayers and trilayers. Centrosymmetric MoS_2 can sustain a nonexpected lift of the degeneracy between bright and dark excitons that can be even stronger than in the single layer, due to the higher difference between the two conduction-band effective masses that predict band-structure calculations. Also, present results reported here shed some light on the origin of nontrivial circular polarization degree of the photoluminescence signal observed in bilayer transition-metal dichalcogenides under circularly polarized excitation light. Regarding the pressure dependence of the indirect band gap, the fact that 2H-MoS_2 can metallize at relatively accessible pressures opens the door for the search of exotic insulator states just before the onset of metallization, for which excitons located at midpoint along the ΓK high-symmetry direction may play a relevant role.

ACKNOWLEDGMENTS

Work in Valencia was supported by the Spanish Government (Grants No. TEC2014-53727-C2-1-R and No. MAT2016-75586-C4-1-P) and the Generalitat Valenciana (Grant No. PROMETEOII/2014/059). Work in Bellaterra was supported by Spanish MINECO (Grants No. FIS2015-64886-C5-3-P and No. FIS2015-64886-C5-4-P), and the Severo Ochoa Centers of Excellence Program (Grants No. SEV-2013-0295 and No. SEV-2015-0496), Generalitat de Catalunya (Grant No. 2017SGR1506 and the CERCA Programme) and by the European Union H2020-EINFRA-5-2015 MaX Center of Excellence (Grant No. 676598). M.B.G. acknowledges Fellowship No. UVINV-PREDOC13-110538 under the program "Atracció de Talent, VLC-CAMPUS" of the University of Valencia.

APPENDIX A: METHODS

1. Optical characterization under pressure

Thin MoS_2 samples with thicknesses varying from 0.13 to 11 μm were cleaved from large single crystals. Due to their weak interlayer bonding, face samples are perpendicular to the c axis. Samples were placed just after the cleavage along with several ruby chips in a 200-μm-diameter hole drilled on a 60-μm-thick Inconel gasket and inserted between the diamonds of a diamond-anvil cell of the membrane type [82]. For measurements in the ultraviolet, visible, and near-infrared range, a mixture of methanol, ethanol, and water in the proportions 16:3:1 was used as hydrostatic pressure transmitting medium. For measurements in the midinfrared, we used KBr as a transmitting medium. The pressure was determined through the ruby luminescence linear scale [83]. Room-temperature optical absorption of the samples was measured as a function of pressure using, for the ultraviolet and visible ranges, a deuterium lamp, spatial filters, reflective objectives, and a multichannel spectrophotometer. For the near-infrared, the light transmitted by the sample was focused on the entrance slit of a Jobin-Yvon M25 monochromator and collected by a Ge photodiode. All optical signals are synchronously measured by using a mechanical chopper and a lock-in amplifier. Optical transmittance measurements of bulk MoS_2 under pressure in the midinfrared were performed by means of Fourier transform infrared spectroscopy, by using an Interspectrum TEO-400 Michelson interferometer module and a noncommercial microsopic optical bench [84]. The obtained absorbance spectra were scaled to the theoretical values expected in the spectral range where the sample is transparent. The absorption coefficient was calculated from the scaled absorbance and the sample thickness, which was obtained from the interference fringe pattern in the transparent region at room pressure. Its variation with pressure was calculated from reported compressibility values [52]. The pressure dependence of the $n_\perp$ has been obtained in the near- and mid-infrared. The $n_\perp$ was measured from transmission interference fringe patterns at normal incidence by using the interference condition. The sample thickness and the interference order at ambient pressure were determined using reported values of the 2H-MoS_2 refractive index [85].

2. Density functional theory calculations

Ab initio calculations were performed within DFT as implemented in the VASP code [86]. Core electrons were treated using the projector augmented wave method [87,88] and wave functions were expanded using a plane-wave basis set with an energy cutoff of 400 eV. For the exchange-correlation functional we used the Ceperley-Alder form of the LDA [81]. Relativistic effects were included by using a scalar relativistic Hamiltonian for both core and valence electrons and adding the spin-orbit coupling (SOC) term in the second-order approximation [89]. A $12 \times 12 \times 3$ **k**-point grid was used to sample the Brillouin zone.

We used experimental a and c lattice parameters and, in order to consider the effects of pressure, we assumed that the 2H-MoS_2 unit cell evolves under compression as reported in Ref. [90]. Once the unit cell was fixed for each pressure the atomic coordinates were relaxed until forces were smaller than 0.01 eV/Å.

The static dielectric matrix was determined using density functional perturbation theory and including local-field effects in the Hartree (random phase) approximation [91,92]. The frequency dependent dielectric matrix was determined by a summation over empty states as explained in Ref. [92]. Since we were only interested in a qualitative picture of the evolution of the frequency dependent dielectric matrix with pressure, its determination was done without taking into account local-field effects and SOC.

APPENDIX B: PRESSURE DEPENDENCE OF CONDUCTION- AND VALENCE-BAND EFFECTIVE MASSES AT THE *K* POINT AND EXCITON MASSES

Figure 8(a) shows the pressure dependence of the effective mass of each one of the conduction and valence bands of 2H-MoS_2 along the ΓK ($m^*_\perp$) and KH ($m^*_\parallel$) high-symmetry directions [see inset of Fig 8(a) for the notation used to label each band]. These effective masses have been obtained by parabolic fitting of the **k** dispersion of each band, as obtained by DFT calculations [as those shown in Fig. 2(a) for 0, 4, and 8 GPa). For convenience, we have adopted the criterion of assigning negative effective-mass values to convex bands. With regard to the valence bands, these results

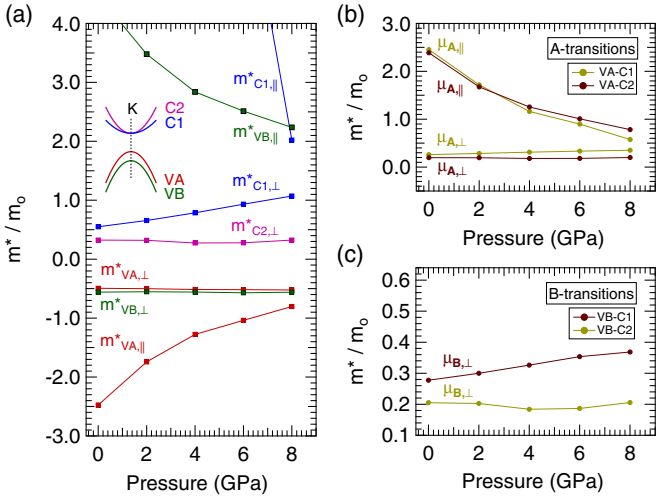

FIG. 8. (a) Pressure dependence of the effective mass of each one (see inset) of the two valence (*VA* and *VB*) and conduction bands (*C*1 and *C*2) of 2H-MoS_2 in the vicinity of the *K* point, as obtained by parabolic fitting of their respective band dispersion calculated by DFT along the Γ*K* ($m^*_\perp$) and *KH* ($m^*_\parallel$) high-symmetry directions. The $m^*_\parallel$ of the *C*2 conduction band is not shown since it exceeds, by more than one order of magnitude, the scale range comprised by this plot, for pressures lower than 8 GPa. (b),(c) Pressure dependence of the exciton reduced mass obtained for each one of the optical transitions that may occur between the *A* and *B* valence bands and the *C*1 and *C*2 conduction bands, respectively. For the *B* transitions, $\mu_{B\parallel}$ values are much higher than these of $\mu_{B\perp}$, justifying their 2D nature.

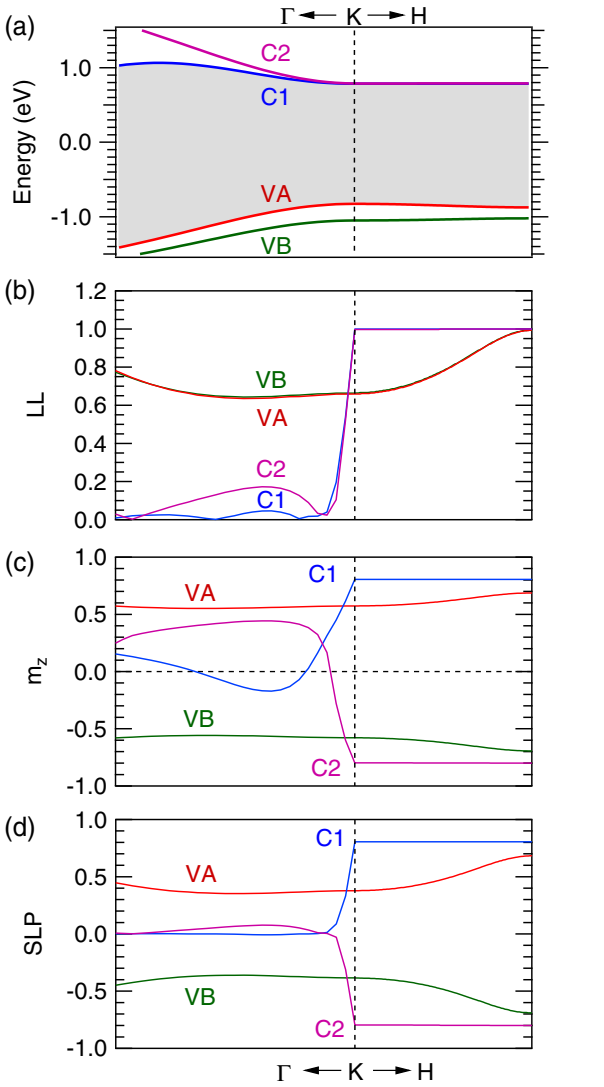

FIG. 9. (a) Dispersion of the valence and conduction bands of 2H-MoS_2 in the vicinity of the *K* point along the Γ*K* and *KH* high-symmetry directions, as calculated by DFT. Grey shaded area represents the band gap. (b) Localization degree of states of the each one of the bands shown in (a) within a ML of 2H-MoS_2, as obtained by DFT calculations performed along the Γ*KH* directions. (c) Spin projection in the *z* direction (i.e., perpendicular to the layers) calculated for conduction- and valence-band states located along the Γ*KH* directions. This spin projection has been calculated for one of the two MLs of the unit cell of 2H-MoS_2. (d) Momentum dependence, along the Γ*KH* directions, of the spin-layer polarization within a particular ML of 2H-MoS_2, as obtained by DFT. In all plots, bands have been labeled as in the inset of Fig. 8(a). Vertical dashed lines indicate the position of the *K* point.

reveal that only their $m^*_\parallel$ experience a notable dependence with pressure. With regard to the two lowest conduction bands at the *K* point, the most remarkable fact is the different trend with pressure obtained for their respective $m^*_\perp$ around the *K* point.

From these results, the pressure dependence of the parallel ($\mu_\parallel$) and perpendicular ($\mu_\perp$) to the *c*-axis exciton reduced mass has been calculated $\mu = (1/m^*_e - 1/m^*_h)^{-1}$ for each one of the optical transitions that may eventually occur between the *A* valence band and the *C*1 and *C*2 conduction bands [Fig. 8(b)] and between the *B* valence band and the *C*1 and *C*2 conduction bands [Fig. 8(c)].

APPENDIX C: SPIN AND BAND LOCALIZATION WITHIN EACH LAYER AS CALCULATED BY DFT

Electronic band-structure calculations shown in Fig. 2(a), as well as those depicted in Fig. 9(a), suggest that conduction-band states defining the direct band gap at the *K* point are strongly localized, whereas those of the two higher valence bands exhibit a moderate localization degree. In order to explore the localization of the bands around the *K* point, which plays a key role for optical-absorption techniques to be able to probe intralayer optical transitions in 2H-MoS_2, we have defined the layer localization (LL) parameter

$$\mathrm{LL} = \frac{|P(Mo_1) - P(Mo_2)|}{|P(Mo_1) + P(Mo_2)|}, \qquad \text{(C1)}$$

where $P(\mathrm{Mo}_i)$ is the projection of the states of a particular band on the Mo atoms of the *i* layer. In this way, states with LL = 1 are completely confined within a particular layer whereas those with LL = 0 are equally extended between two adjacent layers. Figure 9(b) shows the results of these calculations, which clearly reflect that conduction-band states (those of the *C*1 and *C*2 bands) are strongly localized within a particular ML at the *K* point. Conversely, states at the *VA* and *VB* valence bands exhibit a moderate localization within a ML at the *K* point.

Figure 9(c) shows the component of the spin along the z direction (m_z) for states coming from Mo atoms in one of the two MLs of the 2H-MoS_2 unit cell, for each valence and conduction band. For Mo atoms in the other ML of 2H-MoS_2, spin-projection values have an opposite sign. These calculations already reflect the spin band sequence expected for MLs of MoS_2 [see Fig. 3(a)] [12,48,93]. However, in order to evidence the existence of spin-layer polarization, m_z should be different from zero and LL should be close to unity. Therefore, a spin-layer polarization parameter (SLP) defined as SLP $= m_z * \mathrm{LL}$ can be used to quantitatively evaluate the degree of spin-layer polarization of states. Figure 9(d) shows the momentum dependence of the SLP parameter in the vicinity of the K point, which indicates that states involved in direct optical transitions at the K point exhibit a strong spin-layer polarized character, especially those of the conduction bands.

APPENDIX D: PRESSURE DEPENDENCE OF THE STATIC DIELECTRIC CONSTANT

The dielectric function $\varepsilon(\omega) = \mathrm{Re}\,\varepsilon(\omega) + i\,\mathrm{Im}\,\varepsilon(\omega)$ of 2H-MoS_2 has been calculated by DFT theory in the independent particle approximation. The results of these calculations are shown in Fig. 10 under ambient pressure and under pressures of 4 and 8 GPa. From these calculations, it can be observed that, by increasing pressure, the low-energy side of the Im $\varepsilon(\omega)$ tends to shift to lower energies, with a more pronounced effect in the Im $\varepsilon(\omega)$ evaluated in the direction parallel to the c axis [Im $\varepsilon_\parallel(\omega)$]. This effect is consistent with the progressive band-gap closure predicted by DFT (see Sec. IV) and also indicates that the Re $\varepsilon(\omega)$, especially at low energies, increases as pressure does. This observation is relevant for a correct interpretation of the pressure dependence of the exciton absorption coefficient and exciton BE. Consequently, an accurate determination of the electronic contribution to the static dielectric constant [$\varepsilon(0)$] is required. Figure 11 shows the pressure dependence of $\varepsilon(0)$ as calculated by DFT, for the directions perpendicular and parallel to the c-axis [$\varepsilon_\perp(0)$ and $\varepsilon_\parallel(0)$, respectively]. In these calculations, local-field effects have been included, which reveal that both the $\varepsilon_\parallel(0)$ and

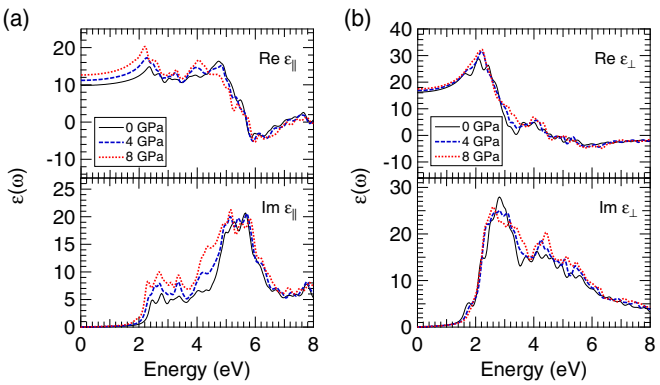

FIG. 10. Calculated real and imaginary parts of the dielectric function in the parallel (a) and perpendicular (b) to the c-axis directions, as obtained by DFT calculations in the independent particle approximation for bulk MoS_2 under ambient conditions and under pressures of 4 and 8 GPa.

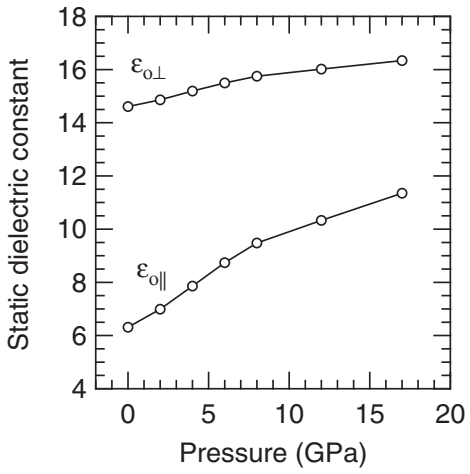

FIG. 11. Pressure dependence of $\varepsilon_\perp(0)$ and $\varepsilon_\parallel(0)$, as obtained by DFT calculations in the local-field approximation.

$\varepsilon_\perp(0)$ tend to increase as the pressure increases from ambient conditions to 17 GPa.

In order to give experimental support to these calculations, we have determined the Re $\varepsilon_\perp(\omega)$ of bulk MoS_2 in the midinfrared (a 3.6-μm-thick MoS_2 sample was employed) and near-infrared regions (a 1.2-μm-thick MoS_2 sample was employed). The absorbance spectra acquired (not shown here) show a Fabry-Pérot interferometry pattern in which the appearance of maxima allows for the determination of the real part of the ordinary refractive index [$n_\perp(\omega)$] for each pressure applied, as they have been shown in Fig. 12. Each one of these $n_\perp(\omega)$ curves shows two asymptotic behavior at both sides of the energy range studied. The low-energy asymptotic behavior can be attributable to a resonance coming from the interaction of

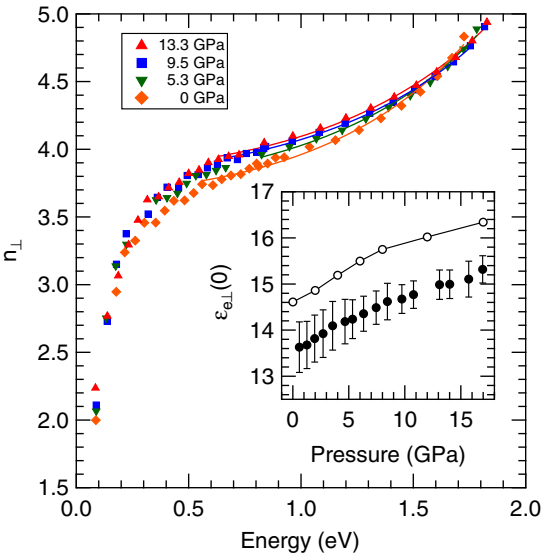

FIG. 12. Dispersion of the real part of the $n_\perp(\omega)$ of 2H-MoS_2 measured under different applied pressures. Solid lines are fitting curves to the experimental $n_\perp(\omega)$ dispersion curves as obtained by using Eq. (D1). The inset shows the pressure dependence of $\varepsilon_\perp(0)$ as obtained from these fittings. The pressure dependence of the $\varepsilon_\perp(0)$ obtained by DFT has been also included in the inset, for comparison purposes.

light with TO phonons, whereas the high-energy one corresponds to the electronic transitions which can be modelled by using an effective transition gap called the Penn gap (E_{gP}) [94]. Focusing ourselves on the electronic contribution to $n_\perp(\omega)$, its energy dependence can be described by

$$n_\perp^2(\omega) = 1 + [\varepsilon_\perp(0) - 1]\left(\frac{E_{gP}^2}{E_{gP}^2 - \omega^2}\right). \quad \text{(D1)}$$

Therefore, by fitting Eq. (D1) to the dispersion $n_\perp(\omega)$ curves shown in Fig. 12, $\varepsilon_\perp(0)$ can be estimated. The inset of Fig. 12 shows the pressure dependence of $\varepsilon_\perp(0)$ as obtained by these fitting procedures. For comparison purposes, we have included the pressure dependence of $\varepsilon_\perp(0)$ as obtained by DFT calculations to evidence that these calculations nicely reproduce the pressure dependence of $\varepsilon_\perp(0)$ obtained experimentally, with a maximum 6% deviation.

[1] H. Zeng, J. Dai, W. Yao, D. Xiao, and X. Cui, Nat. Nanotechnol. **7**, 490 (2012).
[2] X. Xu, W. Yao, D. Xiao, and T. F. Heinz, Nat. Phys. **10**, 343 (2014).
[3] K. F. Mak, K. He, J. Shan, and T. F. Heinz, Nat. Nanotechnol. **7**, 494 (2012).
[4] K. F. Mak, K. L. McGill, J. Park, and P. L. McEuen, Science **344**, 1489 (2014).
[5] Y.-J. Chen, J. D. Cain, T. K. Stanev, V. P. Dravid, and N. P. Stern, Nat. Photonics **11**, 431 (2017).
[6] W.-Y. Tong, S.-J. Gong, X. Wan, and C.-G. Duan, Nat. Commun. **7**, 13612 (2016).
[7] K. Zhang, C. Bao, Q. Gu, X. Ren, H. Zhang, K. Deng, Y. Wu, Y. Li, J. Feng, and S. Zhou, Nat. Commun. **7**, 13552 (2016).
[8] Y. Hsu, A. Vaezi, M. H. Fischer, and E. Kim, Nat. Commun. **8**, 14985 (2017).
[9] N. Zibouche, A. Kuc, J. Musfeldt, and T. Heine, Ann. Phys. **526**, 395 (2014).
[10] W. Han, APL Mater. **4**, 032401 (2016).
[11] X.-X. Zhang, T. Cao, Z. Lu, Y.-C. Lin, F. Zhang, Y. Wang, Z. Li, J. C. Hone, J. A. Robinson, D. Smirnov, S. G. Louie, and T. F. Heinz, Nat. Nanotechnol. **12**, 883 (2017).
[12] J. P. Echeverry, B. Urbaszek, T. Amand, X. Marie, and I. C. Gerber, Phys. Rev. B **93**, 121107 (2016).
[13] Z. Ye, T. Cao, K. O 'brien, H. Zhu, X. Yin, Y. Wang, S. G. Louie, and X. Zhang, Nature (London) **513**, 214 (2014).
[14] M. Baranowski, A. Surrente, D. K. Maude, M. Ballottin, A. A. Mitioglu, P. C. M. Christianen, Y. C. Kung, D. Dumcenco, A. Kis, and P. Plochocka, 2D Mater. **4**, 025016 (2017).
[15] C. Robert, D. Lagarde, F. Cadiz, G. Wang, B. Lassagne, T. Amand, A. Balocchi, P. Renucci, S. Tongay, B. Urbaszek, and X. Marie, Phys. Rev. B **93**, 205423 (2016).
[16] M. Selig, G. Berghäuser, A. Raja, P. Nagler, C. Schüller, T. F. Heinz, T. Korn, A. Chernikov, E. Malic, and A. Knorr, Nat. Commun. **7**, 13279 (2016).
[17] C. Robert, T. Amand, F. Cadiz, D. Lagarde, E. Courtade, M. Manca, T. Taniguchi, K. Watanabe, B. Urbaszek, and X. Marie, Phys. Rev. B **96**, 155423 (2017).
[18] X.-X. Zhang, Y. You, S. Y. F. Zhao, and T. F. Heinz, Phys. Rev. Lett. **115**, 257403 (2015).
[19] K. Marinov, A. Avsar, K. Watanabe, T. Taniguchi, and A. Kis, Nat. Commun. **8**, 1938 (2017).
[20] Z. Wang, L. Zhao, K. F. Mak, and J. Shan, Nano Lett. **17**, 740 (2017).
[21] Z. Y. Zhu, Y. C. Cheng, and U. Schwingenschlögl, Phys. Rev. B **84**, 153402 (2011).
[22] K. Kómider, J. W. González, and J. Fernández-Rossier, Phys. Rev. B **88**, 245436 (2013).
[23] T.-R. Chang, H. Lin, H.-T. Jeng, and A. Bansil, Sci. Rep. **4**, 6270 (2014).
[24] X. Zhang, Q. Liu, J.-W. Luo, A. J. Freeman, and A. Zunger, Nat. Phys. **10**, 387 (2014).
[25] R. Roldán, J. A. Silva-Guillén, M. P. López-Sancho, F. Guinea, E. Cappelluti, and P. Ordejón, Ann. Phys. **526**, 347 (2014).
[26] J. M. Riley, F. Mazzola, M. Dendzik, M. Michiardi, T. Takayama, L. Bawden, C. Granerød, M. Leandersson, T. Balasubramanian, M. Hoesch, T. K. Kim, H. Takagi, W. Meevasana, Ph. Hofmann, M. S. Bahramy, J. W. Wells, and P. D. C. King, Nat. Phys. **10**, 835 (2014).
[27] E. Razzoli, T. Jaouen, M. L. Mottas, B. Hildebrand, G. Monney, A. Pisoni, S. Muff, M. Fanciulli, N. C. Plumb, V. A. Rogalev, V. N. Strocov, J. Mesot, M. Shi, J. H. Dil, H. Beck, and P. Aebi, Phys. Rev. Lett. **118**, 086402 (2017).
[28] P. Ci, Y. Chen, J. Kang, R. Suzuki, H. S. Choe, J. Suh, C. Ko, T. Park, K. Shen, Y. Iwasa, S. Tongay, J. W. Ager, L.-W. Wang, and J. Wu, Nano Lett. **17**, 4982 (2017).
[29] A. R. Beal, J. C. Knights, and W. Y. Liang, J. Phys. C Solid State Phys. **5**, 3540 (1972).
[30] B. L. Evans and P. A. Young, Proc. R. Soc. A Math. Phys. Eng. Sci. **298**, 74 (1967).
[31] A. Molina-Sánchez, D. Sangalli, K. Hummer, A. Marini, and L. Wirtz, Phys. Rev. B **88**, 045412 (2013).
[32] A. Molina-Sánchez, K. Hummer, and L. Wirtz, Surf. Sci. Rep. **70**, 554 (2015).
[33] R. J. Elliott, Phys. Rev. **108**, 1384 (1957).
[34] Y. Toyozawa, Prog. Theor. Phys. **27**, 89 (1962).
[35] N. Saigal, V. Sugunakar, and S. Ghosh, Appl. Phys. Lett. **108**, 132105 (2016).
[36] A. R. Goñi and K. Syassen, Semicond. Semimetals **54**, 247 (1998).
[37] A. R. Goñi, A. Cantarero, K. Syassen, and M. Cardona, Phys. Rev. B **41**, 10111 (1990).
[38] G. H. Li, A. R. Goñi, K. Syassen, and M. Cardona, Phys. Rev. B **49**, 8017 (1994).
[39] M. Gauthier, A. Polian, J. M. Besson, and A. Chevy, Phys. Rev. B **40**, 3837 (1989).
[40] F. J. Manjón, D. Errandonea, A. Segura, V. Muñoz, G. Tobías, P. Ordejón, and E. Canadell, Phys. Rev. B **63**, 125330 (2001).
[41] J. F. Sánchez-Royo, A. Segura, and V. Muñoz, Phys. Status Solidi A **151**, 257 (1995).
[42] A. R. Goñi, A. Cantarero, U. Schwarz, K. Syassen, and A. Chevy, Phys. Rev. B **45**, 4221 (1992).
[43] M. Shinada and S. Sugano, J. Phys. Soc. Jpn. **21**, 1936 (1966).
[44] A. R. Goñi, K. Syassen, Y. Zhang, K. Ploog, A. Cantarero, and A. Cros, Phys. Rev. B **45**, 6809 (1992).

[45] R. Le Toullec, N. Piccioli, and J. C. Chervin, Phys. Rev. B **22**, 6162 (1980).

[46] C. H. Ho, C. S. Wu, Y. S. Huang, P. C. Liao, and K. K. Tiong, J. Phys.: Condens. Matter **10**, 9317 (1998).

[47] Q. Sun, L. Yadgarov, R. Rosentsveig, G. Seifert, R. Tenne, and J. L. Musfeldt, ACS Nano **7**, 3506 (2013).

[48] D. W. Latzke, W. Zhang, A. Suslu, T. R. Chang, H. Lin, H. T. Jeng, S. Tongay, J. Wu, A. Bansil, and A. Lanzara, Phys. Rev. B **91**, 235202 (2015).

[49] F. Dybała, M. P. Polak, J. Kopaczek, P. Scharoch, K. Wu, S. Tongay, and R. Kudrawiec, Sci. Rep. **6**, 26663 (2016).

[50] H. Guo, T. Yang, P. Tao, Y. Wang, and Z. Zhang, J. Appl. Phys. **113**, 013709 (2013).

[51] L. Hromadová, R. Martoňák, and E. Tosatti, Phys. Rev. B **87**, 144105 (2013).

[52] H. Peelaers and C. G. Van de Walle, J. Phys. Chem. C **118**, 12073 (2014).

[53] R. Coehoorn, C. Haas, and R. A. de Groot, Phys. Rev. B **35**, 6203 (1987).

[54] G. A. N. Connell, J. A. Wilson, and A. D. Yoffe, J. Phys. Chem. Solids **30**, 287 (1969).

[55] H. P. Komsa and A. V. Krasheninnikov, Phys. Rev. B **86**, 241201(R) (2012).

[56] J. A. Wilson and A. D. Yoffe, Adv. Phys. **18**, 193 (1969).

[57] B. Gerlach and J. Pollmann, Phys. Status Solidi **67**, 93 (1975).

[58] J. Martinez-Pastor, A. Segura, C. Julien, and A. Chevy, Phys. Rev. B **46**, 4607 (1992).

[59] S. Wu, J. S. Ross, G. Bin Liu, G. Aivazian, A. Jones, Z. Fei, W. Zhu, D. Xiao, W. Yao, D. Cobden, and X. Xu, Nat. Phys. **9**, 149 (2013).

[60] A. M. Jones, H. Yu, J. S. Ross, P. Klement, N. J. Ghimire, J. Yan, D. G. Mandrus, W. Yao, and X. Xu, Nat. Phys. **10**, 130 (2014).

[61] B. Zhu, H. Zeng, J. Dai, Z. Gong, and X. Cui, Proc. Natl. Acad. Sci. **111**, 11606 (2014).

[62] J. Xia, X. Wang, B. K. Tay, S. Chen, Z. Liu, J. Yan, and Z. Shen, Nano Res. **10**, 1618 (2017).

[63] I. Aharonovich, D. Englund, and M. Toth, Nat. Photonics **10**, 631 (2016).

[64] Y. M. He, O. Iff, N. Lundt, V. Baumann, M. Davanco, K. Srinivasan, S. Höfling, and C. Schneider, Nat. Commun. **7**, 13409 (2016).

[65] A. Branny, G. Wang, S. Kumar, C. Robert, B. Lassagne, X. Marie, B. D. Gerardot, and B. Urbaszek, Appl. Phys. Lett. **108**, 142101 (2016).

[66] P. Tonndorf, R. Schmidt, R. Schneider, J. Kern, M. Buscema, G. A. Steele, A. Castellanos-Gomez, H. S. J. van der Zant, S. Michaelis de Vasconcellos, and R. Bratschitsch, Optica **2**, 347 (2015).

[67] M. Koperski, K. Nogajewski, A. Arora, V. Cherkez, P. Mallet, J.-Y. Veuillen, J. Marcus, P. Kossacki, and M. Potemski, Nat. Nanotechnol. **10**, 503 (2015).

[68] A. Srivastava, M. Sidler, A. V. Allain, D. S. Lembke, A. Kis, and A. Imamoğlu, Nat. Nanotechnol. **10**, 491 (2015).

[69] S. Kumar, A. Kaczmarczyk, and B. D. Gerardot, Nano Lett. **15**, 7567 (2015).

[70] S. Kumar, A. Branny, R. Proux, and B. D. Gerardot, Nat. Commun. **8**, 15053 (2017).

[71] B. R. Carvalho, Y. Wang, S. Mignuzzi, D. Roy, M. Terrones, C. Fantini, V. H. Crespi, L. M. Malard, and M. A. Pimenta, Nat. Commun. **8**, 14670 (2017).

[72] M. Peña-Álvarez, E. Del Corro, Á. Morales-García, L. Kavan, M. Kalbac, and O. Frank, Nano Lett. **15**, 3139 (2015).

[73] X. Fan, C.-H. Chang, W. T. Zheng, J.-L. Kuo, and D. J. Singh, J. Phys. Chem. C **119**, 10189 (2015).

[74] B. Liu, Y. Han, C. Gao, Y. Ma, G. Peng, B. Wu, C. Liu, Y. Wang, T. Hu, X. Cui, W. Ren, Y. Li, N. Su, H. Liu, and G. Zou, J. Phys. Chem. C **114**, 14251 (2010).

[75] D. Jérome, T. M. Rice, and W. Kohn, Phys. Rev. **158**, 462 (1967).

[76] M. Rifliková, R. Martoňák, and E. Tosatti, Phys. Rev. B **90**, 035108 (2014).

[77] A. P. Nayak, S. Bhattacharyya, J. Zhu, J. Liu, X. Wu, T. Pandey, C. Jin, A. K. Singh, D. Akinwande, and J.-F. Lin, Nat. Commun. **5**, 3731 (2014).

[78] Z. H. Chi, X. M. Zhao, H. Zhang, A. F. Goncharov, S. S. Lobanov, T. Kagayama, M. Sakata, and X. J. Chen, Phys. Rev. Lett. **113**, 036802 (2014).

[79] Y. Zhuang, L. Dai, L. Wu, H. Li, H. Hu, K. Liu, L. Yang, and C. Pu, Appl. Phys. Lett. **110**, 122103 (2017).

[80] S. Wang, J. Zhang, D. He, Y. Zhang, L. Wang, H. Xu, X. Wen, H. Ge, and Y. Zhao, J. Phys. Chem. Solids **75**, 100 (2014).

[81] D. M. Ceperley and B. J. Alder, Phys. Rev. Lett. **45**, 566 (1980).

[82] J. C. Chervin, B. Canny, J. M. Besson, and P. Pruzan, Rev. Sci. Instrum. **66**, 2595 (1995).

[83] G. J. Piermarini, S. Block, J. D. Barnett, and R. A. Forman, J. Appl. Phys. **46**, 2774 (1975).

[84] V. Panchal, A. Segura, and J. Pellicer-Porres, High Press. Res. **31**, 445 (2011).

[85] A. R. Beal and H. P. Hughes, J. Phys. C: Solid State Phys. **12**, 881 (1979).

[86] G. Kresse and J. Furthmüller, Phys. Rev. B **54**, 11169 (1996).

[87] P. E. Blöchl, Phys. Rev. B **50**, 17953 (1994).

[88] G. Kresse and D. Joubert, Phys. Rev. B **59**, 1758 (1999).

[89] S. Steiner, S. Khmelevskyi, M. Marsmann, and G. Kresse, Phys. Rev. B **93**, 224425 (2016).

[90] N. Bandaru, R. S. Kumar, D. Sneed, O. Tschauner, J. Baker, D. Antonio, S.-N. Luo, T. Hartmann, Y. Zhao, and R. Venkat, J. Phys. Chem. C **118**, 3230 (2014).

[91] S. Baroni and R. Resta, Phys. Rev. B **33**, 7017 (1986).

[92] M. Gajdoš, K. Hummer, G. Kresse, J. Furthmüller, and F. Bechstedt, Phys. Rev. B **73**, 045112 (2006).

[93] J. A. Miwa, S. Ulstrup, S. G. Sørensen, M. Dendzik, A. G. Čabo, M. Bianchi, J. V. Lauritsen, and Ph. Hofmann, Phys. Rev. Lett. **114**, 046802 (2015).

[94] D. R. Penn, Phys. Rev. **128**, 2093 (1962).